nature communications

Article

https://doi.org/10.1038/s41467-025-58502-1

Perfect anomalous refraction metasurfaces empowered half-space optical beam scanning

Received: 31 May 2024

Accepted: 20 March 2025

Published online: 01 April 2025

Check for updates

Tao He[1,2,3,4,5,6], Dongdong Li[1,2,3,4,5,6], Chengfeng Li[1,2,3,4,5], Haigang Liang[1,2,3,4,5], Chao Feng[1,2,3,4,5], Jingyuan Zhu[1,2,3,4,5], Lingyun Xie[1,2,3,4,5], Siyu Dong[1,2,3,4,5], Yuzhi Shi[1,2,3,4,5], Xiong Dun[1,2,3,4,5], Zeyong Wei[1,2,3,4,5], Zhanshan Wang[1,2,3,4,5] ✉ & Xinbin Cheng[1,2,3,4,5] ✉

Metasurface-based optical beam scanning devices are gaining attention in optics and photonics for their potential to revolutionize light detection and ranging systems. However, achieving anomalous refraction with perfect efficiency (>99%) remains challenging, limiting the efficiency and field of view (FOV) of metasurface-based optical beam scanning devices. Here, we introduce a paradigm for achieving perfect anomalous refraction by augmenting longitudinal degrees of freedom arousing a multiple scattering process to optimize symmetry breaking. An all-dielectric quasi-three-dimensional subwavelength structure (Q3D-SWS), composed of a purposely designed multilayer film and a dielectric metasurface separated by a spacer, is proposed to eliminate reflection loss and spurious diffraction, achieving >99% anomalous refraction efficiency. By independently rotating two cascaded Q3D-SWSs, we experimentally showcase half-space optical beam scanning, achieving a FOV of 144° × 144°, with a maximum efficiency exceeding 86%. Our results open new avenues for high-efficiency metasurfaces and advances applications in light detection and ranging systems.

The emergence of metasurfaces, a class of planar metamaterials that transcends natural materials, has given rise to a myriad of innovative approaches to manipulate light[1,2]. Thus far, metasurfaces have been employed to demonstrate a variety of compact optical components with significant capabilities, including anomalous deflections of light[3,4], metalens imaging[5,6], holographic imaging[7,8], and other applications[9,10]. In recent years, the advancement of metasurfaces has sparked numerous applications and attracted widespread attention[11–14]. Metasurface-based optical beam scanning stands out as one of the most extensively studied devices[15–20] owing to its crucial roles in monitoring atmospheric conditions, environmental observations, autonomous vehicles, artificially intelligent robots, and unmanned aerial vehicle reconnaissance[21–24].

A metasurface-based optical beam scanning device typically deflects a beam in different directions at different times to enable ranging[25]. Various tunable materials[25–31], including indium tin oxide[25,32], liquid crystals[16,31], multiple quantum wells[19,30], and monolayer molybdenum diselenide[33], have been extensively integrated into anomalous deflection metasurfaces. One-dimensional continuous laser scanning is performed with a maximum laser deflection angle of approximately 4° by electrically regulating indium tin oxide[25], yet the efficiency is less than 1%. The integration of liquid crystals with metasurfaces was

[1]Institute of Precision Optical Engineering, School of Physics Science and Engineering, Tongji University, Shanghai, China. [2]MOE Key Laboratory of Advanced Micro-Structured Materials, Shanghai, China. [3]Shanghai Frontiers Science Center of Digital Optics, Shanghai, China. [4]Shanghai Professional Technical Service Platform for Full-Spectrum and High-Performance Optical Thin Film Devices and Applications, Shanghai, China. [5]Shanghai Institute of Intelligent Science and Technology, Tongji University, Shanghai, China. [6]These authors contributed equally: Tao He, Dongdong Li. ✉e-mail: wangzs@tongji.edu.cn; chengxb@tongji.edu.cn

proposed to enable one-dimensional dynamic deflection[31], yielding a maximum refraction angle of 11° and an efficiency of 35%. These materials facilitate space–time modulation of the amplitude and phase profiles in both reflection and transmission modes at the subwavelength scale[27,34], allowing for precise laser beam control. This architecture provides considerable degrees of freedom, leading to significant advancements in dynamic light beam manipulation. However, the challenge of simultaneously achieving high efficiency and a large field of view (FOV) in beam scanning persists, limiting its application in fields such as spanning from landscape mapping[23], autonomous driving[24], and beyond[21]. Remarkably, while transmission mode presents advantages in system simplification and integration, most tunable metasurface-based optical beam scanning devices currently operate in reflection and one-dimensional modes[17,20], largely owing to the greater challenges associated with achieving high-efficiency metasurfaces in transmission mode.

The performance of the anomalous deflection metasurface directly influences the efficiency and FOV of metasurface-based optical beam scanning devices. Recent work has emphasized that the nonlocal response must be considered to achieve high-efficiency anomalous deflection[35,36]. Various auxiliary fields were utilized to perfectly suppress spurious diffraction in reflection mode[37,38]. However, achieving perfect anomalous deflection in transmission mode is more challenging than in reflection mode, as it requires the elimination of five spurious diffraction ports for perfect anomalous refraction, whereas only two for perfect anomalous reflection. Several metasurface architectures[39–46], including freeform geometries[39] that maximize the in-plane degree of freedom, have been proposed to increase the anomalous refraction efficiency by controlling mode interference but still encounter difficulties related to reflection loss. To date, achieving perfect anomalous refraction remains an ongoing challenge, highlighting the urgent need for new physical paradigms. This dilemma constrains both the efficiency and FOV of metasurface-based optical beam scanning devices.

Here, we present a paradigm for achieving perfect anomalous refraction by augmenting longitudinal degrees of freedom, arousing a multiple scattering process to optimize symmetry breaking. We demonstrate perfect anomalous refraction for the first time, with a polarization-insensitive absolute efficiency exceeding 99%, through the construction of an all-dielectric quasi-three-dimensional subwavelength structure (Q3D-SWS), which is composed of a purposely designed multilayer film and a dielectric metasurface separated by a dielectric spacer. To achieve perfect anomalous refraction, a multilayer film with special amplitude and phase responses, which exhibits high transmittance to zeroth-order propagating waves and high reflectance to first-order propagating waves, was designed to completely suppress reflection loss and spurious diffraction. To demonstrate high-efficiency optical beam scanning with a large FOV, we adopt a widely used mechanical beam steering method, as illustrated in Fig. 1a, which experimentally shows half-space optical beam scanning with a FOV of 144° × 144° and a maximum efficiency exceeding 86%. Our results are expected to have practical applications in light detection and ranging systems and equipment.

Results

Model and theory of a quasi-three-dimensional subwavelength structure realizing perfect anomalous refraction

To realize a high-efficiency metasurface-based beam scanning device, the primary goal is to achieve high-efficiency anomalous refraction. The question at hand is: What type of metasurface can achieve high-efficiency anomalous refraction at optical frequencies? Anomalous refraction fundamentally involves asymmetric diffraction, highlighting that breaking symmetry is crucial to achieving high-efficiency anomalous refraction. Metasurfaces featuring freeform geometries designed through topological optimization provide the greatest degree of freedom to break in-plane asymmetry. However, single-layer metasurfaces with solely lateral degrees of freedom struggle to achieve perfect anomalous refraction in the optical frequency domain, primarily due to the inevitable reflection loss and/or spurious diffraction[39–47].

In response to these challenges, we propose the concept of augmenting the longitudinal degrees of freedom to optimize symmetry breaking. We construct a Q3D-SWS consisting of an equivalent upper interface and an equivalent bottom interface separated by a dielectric spacer, as shown in Fig. 1b. When incident light I_0 is incident upon the Q3D-SWS, some of the incident light is reflected directly back into incident medium 1, which is recorded as R_0. The remaining transmitted light, denoted as $t_{21}I_0$, passes through the bottom interface into the spacer (medium 2). The light in the spacer undergoes phase accumulation p and then interacts with the upper interface. The phase accumulation of light is given by e^{ikh}, where k represents the wave vector in the spacer and h denotes the thickness of the spacer. Similarly, a portion of the light is reflected into the spacer layer, whereas the rest is transmitted into exit medium 3. The reflected light is recorded as $r_u pt_{21}I_0$, and the transmitted light $T_1 = t_{32}pt_{21}I_0$. The reflected light then traverses the spacer layer and interacts with the bottom interface again. Some of the light passes through the bottom interface into medium 1 and is recorded as R_1. R_1 is given by $t_{12}pr_upt_{21}I_0$. The remaining reflected light $r_bpr_upt_{21}I_0$ will traverse the spacer layer repeatedly and undergo repeated interactions with the two interfaces. These interactions at the upper interface cause mode leakage, resulting in the formation of transmitted light T_n, where $T_n = t_{32}(pr_bpr_u)^{n-1}pt_{21}I_0$, whereas those at the bottom interface lead to the formation of R_n, where $R_n = t_{12}(pr_upr_b)^{n-1}pr_upt_{21}I_0$ ($n > 0$). Ultimately, the overall reflection and transmission coefficients of the Q3D-SWS can be expressed as

$$R = \sum_{i=0}^{i=n} R_i = R_0 + t_{12}\left(\mathrm{I} - pr_upr_b\right)^{-1}pr_upt_{21}. \quad (1)$$

$$T = \sum_{i=0}^{i=n} T_i = t_{32}\left(\mathrm{I} - pr_bpr_u\right)^{-1}pt_{21}. \quad (2)$$

Notably, all transmission and reflection coefficients in this paper are presented in matrix form, representing various orders of electromagnetic waves, due to the existence of a periodic metasurface, and the symbol I represents a unit matrix. For example, in a three-port system under normal incident ($I_0 = [0; 1; 0]$) in this work, the anomalous reflection and refraction efficiencies are calculated as $[R^{-1,eff}; R^{0,eff}; R^{+1,eff}] = |RI_0|^2$ and $[T^{-1,eff}; T^{0,eff}; T^{+1,eff}] = |TI_0|^2$. The superscript denotes the diffraction order. Based on the above formula, the anomalous deflection process of the Q3D-SWS can be understood as a form of multiple scattering. To realize perfect anomalous refraction, we have to make $[R^{-1,eff}; R^{0,eff}; R^{+1,eff}] = |RI_0|^2 = [0; 0; 0]$ and $[T^{-1,eff}; T^{0,eff}; T^{+1,eff}] = |TI_0|^2 = [0; 0; 1]$. The anomalous reflection and refraction efficiencies can be controlled by both the bottom interface (t_{21}, t_{12}, r_b, R_0) and the upper interface (t_{32}, r_u). Obviously, the scattering coefficients of the bottom interface, especially the reflection coefficient r_b, have a more significant effect on the anomalous reflection and refraction efficiencies of the met-system. However, the reflection coefficient r_b is a 3 × 3 complex matrix that is difficult to manipulate. Therefore, we propose the use of multilayer films for constructing the bottom interface and a metasurface for constructing the upper interface, as shown in Fig. 1c. The multilayer films have a simplified reflection coefficient where $r_b = [r^1e^{i\varphi^1}, 0, 0; 0, r^0e^{i\varphi^0}, 0; 0, 0, r^1e^{i\varphi^1}]$, which is conducive to purposeful regulation. (r^0, φ^0) and (r^1, φ^1) represent the reflection amplitude and phase of the zeroth- and first-order propagating waves in the spacer layer, respectively. By designing a multilayer film with a fine-tuned combination of (r^0, φ^0) and (r^1, φ^1), it is feasible to

https://doi.org/10.1038/s41467-025-58502-1

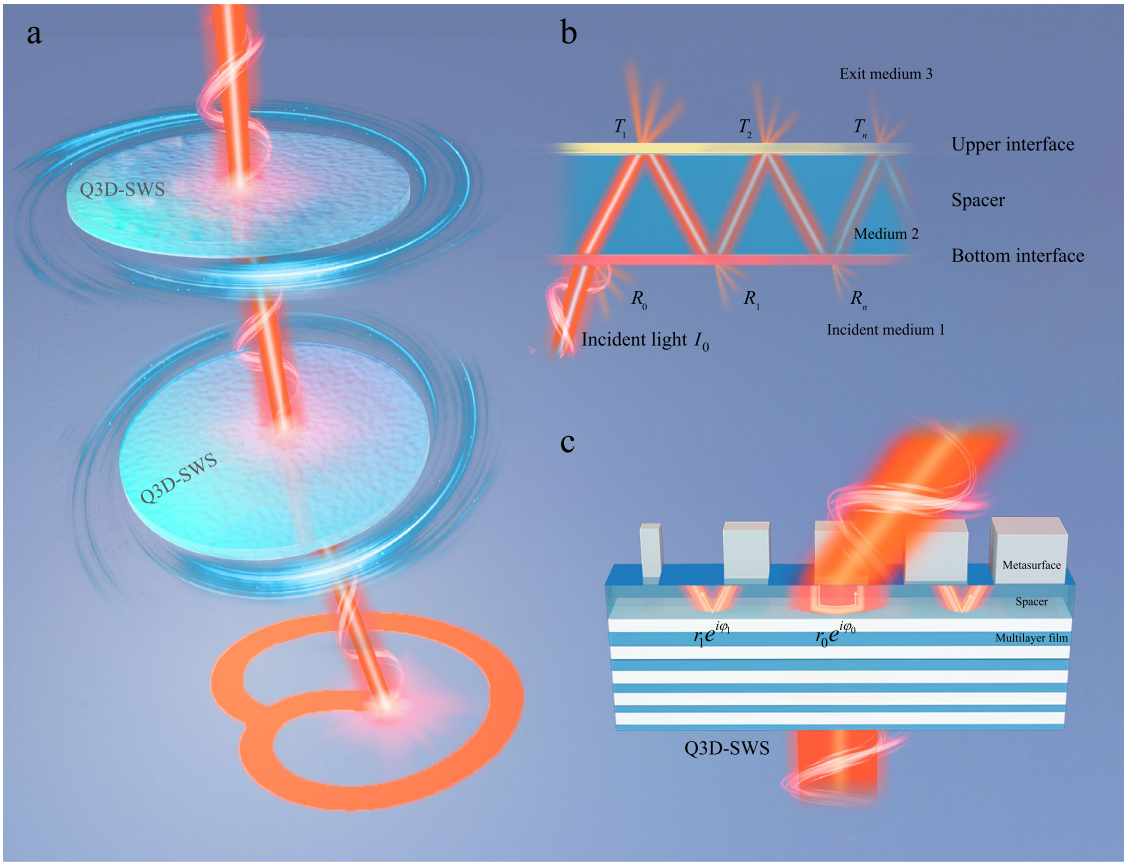

Fig. 1 | High-efficiency half-space beam scanning device based on an all-dielectric quasi-three-dimensional subwavelength structure. a Conceptual schematic of the beam scanning device. The device can achieve high-efficiency two-dimensional scanning by independently rotating two cascaded perfect anomalous refraction metasurfaces. With proper selection of the deflection angles of the metasurfaces, the scanning range can cover the entire space forward. **b** Schematic diagram of the multiple scattering process. The coefficients t_{ji} represent the transmission coefficients of the bottom and upper interfaces when a plane wave is incident from medium i and exits into medium j. r_u *and* r_b represent the reflection coefficients of the upper and bottom interfaces, respectively. These coefficients are complex numbers that include both amplitude and phase responses. **c** Perfect anomalous refraction based on the quasi-three-dimensional subwavelength structure. Within the quasi-three-dimensional subwavelength structure, a multilayer film is utilized to completely suppress reflection loss and spurious diffraction. In the spacer layer, the zeroth- and first-order propagating waves are stimulated by the metasurface and regulated by the amplitude and phase responses (r^0, r^1, φ^0, φ^1) of the multilayer film.

completely suppress reflection loss and spurious diffraction, thereby achieving perfect anomalous refraction. This feasibility will be demonstrated later.

Design and characterization of the quasi-three-dimensional subwavelength structure. The design process for a Q3D-SWS achieving perfect anomalous refraction involves two steps: first, a gradient metasurface is designed to achieve high relative efficiency; second, a multilayer film with specific reflection coefficients for zeroth- and first-order propagating waves in the spacer is designed to minimize reflection loss and deflect all incident light in the predetermined direction. An illustration of the gradient metasurface is shown in Fig. 2a. The metasurface consists of pillar arrays on a silicon oxide substrate. The periods of the unit cell and metasurface are 460 nm and 2300 nm, respectively. The length and width of the 5 pillars are (111 nm, 197 nm), (241 nm, 216 nm), (310 nm, 270 nm), (314 nm, 317 nm), and (345 nm, 380 nm), and the height is 940 nm. Notably, the geometric parameters of the gradient metasurface were obtained by optimizing the result derived from the gradient phase principle. Figure 2a illustrates the anomalous refraction in the 1300–1600 nm range, in terms of both relative and absolute efficiency, for TE polarization. The results and design processes for TM polarization are presented in Supplementary Information 1, as they are similar to those for TE polarization. The relative efficiency for TE polarization reaches a remarkable 95% at 1550 nm, whereas the absolute efficiency is comparatively lower at 76%. The low absolute efficiency can be attributed to both reflection loss and spurious diffraction. For TE polarization, the reflection loss and spurious diffraction values are approximately 20% and 4%, respectively (see more details in Supplementary Information 2 and 3). Despite the possibility of mitigating the aforementioned energy loss through the use of advanced optimization algorithms, it is still far from achieving perfect anomalous refraction.

As described in the previous section, reflection loss and spurious diffraction can be completely suppressed by designing a special multilayer film. The relations between the reflection amplitudes r^0 and r^1 and the transmittance are shown in Fig. 2b. The high transmittances of the Q3D-SWS are located at the top left corner, corresponding to a small value of r^0 and a large value of r^1. In other words, the conditions for suppressing reflection loss are high transmittance to zeroth-order propagating waves and high reflectance to first-order propagating waves. The results are interesting because the condition that inhibits reflection loss, as is commonly believed, is high transmission (which is a small value of both r^0 and r^1). Finally, we chose 0.06 and 1 as the values of r^0 and r^1, respectively. Under this condition, we calculate the absolute efficiency while varying the reflection phases φ^0 and φ^1, as illustrated in Fig. 2c. Notably, the absolute efficiency is primarily

https://doi.org/10.1038/s41467-025-58502-1

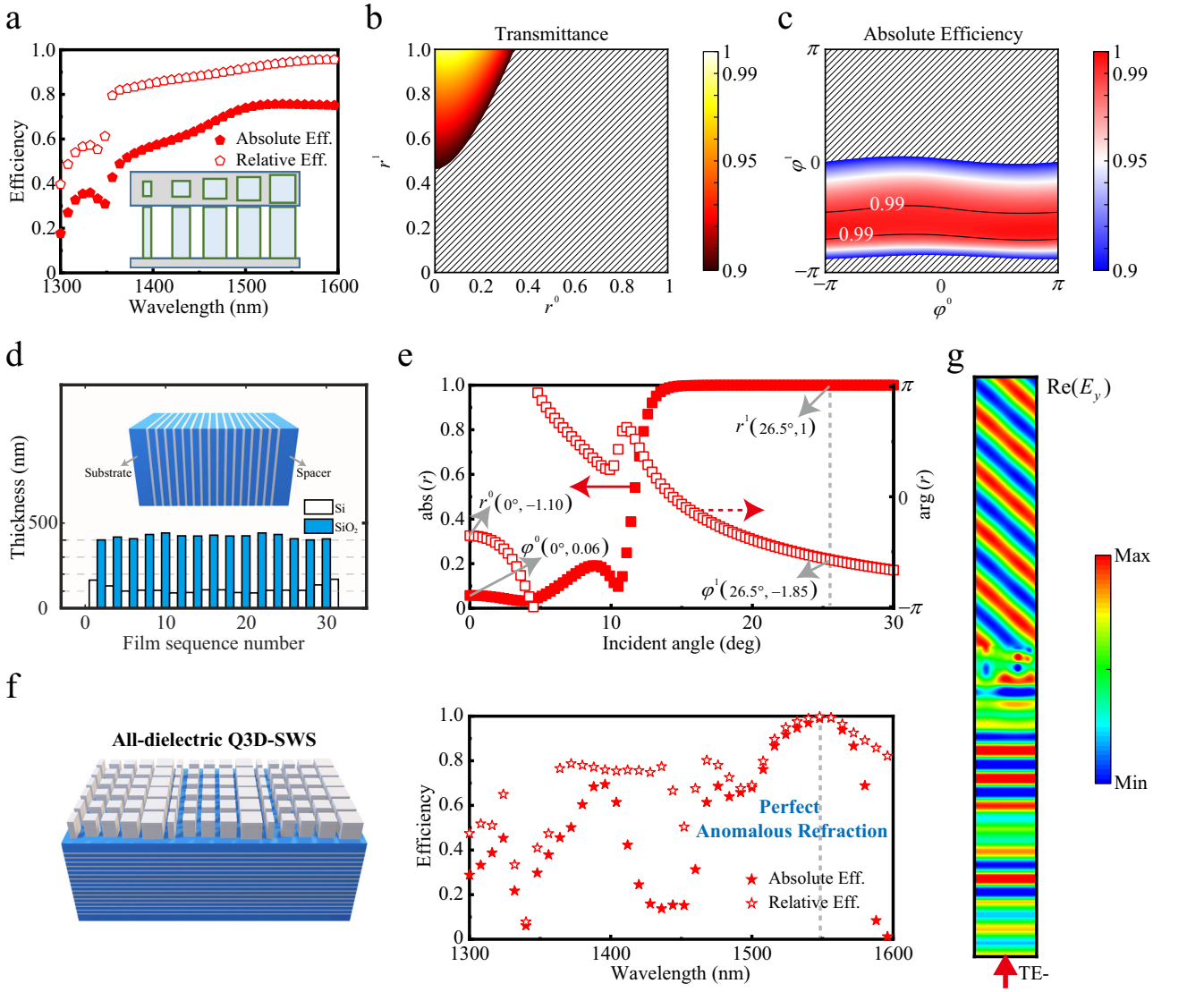

Fig. 2 | Design of perfect anomalous refraction via the quasi-three-dimensional subwavelength structure. a Schematic diagram and spectra of the single-layer metasurface. **b** Relation of the amplitude responses r^0 and r^1 with respect to the transmittance. **c** Relation of the phase responses φ^0 and φ^1 with respect to the absolute efficiency. The contour lines indicate the areas with an efficiency of 99%. The spacer is set to a thickness of 377 nm, but its effect is negligible as the propagating phases can be compensated by the reflection phases. **d** Schematic diagram and thickness of the multilayer film. **e** The reflection amplitude and phase of the multilayer film. The propagation angles of the zeroth- and first-order propagating waves are 0° and 26.5°, respectively. **f** Schematic diagram and spectra of the quasi-three-dimensional subwavelength structure. **g** The electric field distribution of the quasi-three-dimensional subwavelength structure for TE polarization at a wavelength of 1550 nm. The spectra and electric field distributions both confirm the realization of perfect anomalous refraction for TE polarization at 1550 nm.

controlled by φ^1, as it directly influences the interference of the first-order reflection. There is a wide range of parameters through which anomalous refraction can be achieved with an absolute efficiency exceeding 99%. With a φ^1 of approximately −1.8, perfect anomalous refraction can be achieved. Then, a meticulously engineered multilayer film was designed to achieve special reflection amplitudes and phases. A schematic diagram and thickness of the multilayer film are shown in Fig. 2d. This multilayer film consists of 31 layers formed by alternating stacking of Si and SiO_2 materials (see more details in Supplementary Information 4). Figure 2e presents the reflection amplitude and phase of the films, with the incident medium set as the SiO_2 spacer. The exact values of (0.06, 1) and (−1.10, −1.85) for (r^0, r^1) and (φ^0, φ^1), respectively, fulfill the criteria for achieving perfect anomalous refraction.

The multilayer film, spacer, and metasurface are combined to form the Q3D-SWS, as shown in Fig. 2f. Figure 2f also shows the relative and absolute anomalous refraction efficiencies of the Q3D-SWS. Both the relative and absolute efficiencies can reach 99%, thereby achieving perfect anomalous refraction. To further validate the performance of the Q3D-SWS, we present the electric field distribution for TE polarization in Fig. 2g and the magnetic field distribution for TM polarization in Supplementary Information 1, both at the designed wavelength of 1550 nm. The incident light was entirely deflected into the predetermined direction, exhibiting negligible reflection loss and spurious diffraction for both TE and TM polarization. It is worth mentioning that perfect anomalous refraction occurs exclusively at 1550 nm; however, this marks the beginning of the potential for broadband perfect anomalous refraction.

The preparation of the Q3D-SWS sample involved a multilayer film deposition process and metasurface fabrication technology. Magnetron sputtering deposition, electron beam lithography, and inductively coupled reactive ion etching were used for deposition, patterning, and etching, respectively (see more details in "Methods" section and Supplementary Information 4–6). Figure 3a, b show top- and side-view

https://doi.org/10.1038/s41467-025-58502-1

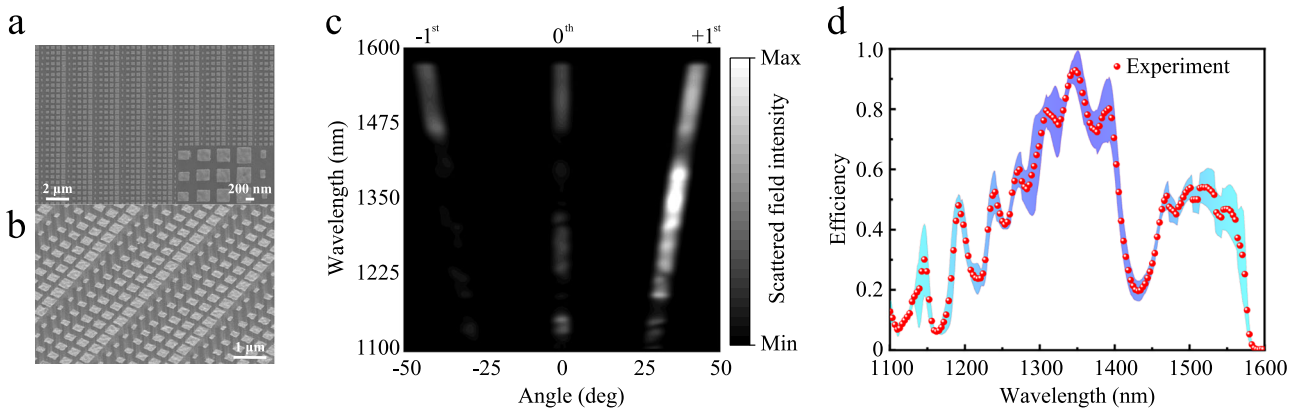

Fig. 3 | Preparation and characterization of the quasi-three-dimensional subwavelength structure. a Scanning electron microscopy top-view image of the quasi-three-dimensional subwavelength structure sample. **b** Scanning electron microscopy side-view image of the quasi-three-dimensional subwavelength structure sample. **c** Far-field scattered light from all angles of the sample. The scattered field predominantly exhibits +1st-order diffraction, indicating high-efficiency anomalous refraction. **d** Broadband anomalous refraction efficiency of the quasi-three-dimensional subwavelength structure sample. The colored band represents the test error bar. The experimental standard deviations of the anomalous refraction efficiencies are 6.7% at 1350 nm and 7.6% at 1550 nm.

scanning electron microscopy (SEM) images of the sample. We conducted spectral tests in R1, an angle-resolved spectrum system (Ideaoptics, China), in a dark room. Angle resolution in the R1 system is achieved through the mechanical rotation of the receiver. During the tests, the diffracted light was consistently incident perpendicularly to the receiving light path and was subsequently received by the receiver. Therefore, the mechanical rotation of the receiver is not the primary cause of spectral testing errors, and its effect can be neglected. In the test, the intensity of the incident light at different wavelengths was detected through the substrate without any multilayer film or metasurface. The intensities of $+1^{st}$-, -1^{st}-, and 0^{th}-order light were subsequently detected simultaneously for all the wavelengths, as shown in Fig. 3c, enabling the determination of the anomalous refraction efficiency. Figure 3d displays the obtained absolute anomalous refraction efficiency in the broadband region, as observed in the spectral test. The fabricated sample demonstrated an anomalous refraction efficiency of approximately 47% at 1550 nm. The highest anomalous refraction efficiency was 93% at 1350 nm. Notably, the Q3D-SWS does not exhibit similar behavior at 1300–1400 nm as it does at 1550 nm. In our experiment, we employed a halogen lamp to generate broadband light and assess the broadband responses of the Q3D-SWS sample, thereby ruling out any wavelength deviation as a cause for the experimental results. The deviation between the design and experiment can be attributed mainly to fabrication errors arising from the lithography and etching processes. To investigate potential spectral shifts due to fabrication errors, we calculated the broadband efficiency based on parameters obtained from SEM characterization, represented by the black line in Fig. S10 in Supplementary Information 7. The good agreement between the SEM-based simulations and experimental results suggests that the discrepancies between the design and experiment primarily arise from fabrication errors during the lithography and etching processes. Besides, we have also calculated the anomalous refraction efficiency of the Q3D-SWS at different incident angles for TE polarization, as shown in Fig. S11 in Supplementary Information 8. Our analysis indicates that the anomalous refraction efficiency decreases significantly as the incident angle deviates from normal incidence. This characteristic may also affect the efficiency of our experimental tests. Therefore, the discrepancies observed between the SEM-based simulations and the experimental data are largely attributed to fabrication errors of the multilayer films and test errors in the spectral measurements. The efficiency can be further increased through the optimization of the spectral test and preparation process.

Demonstration of beam scanning based on cascaded quasi-three-dimensional subwavelength structures

Considering the substantial impact of the anomalous deflection metasurface on the performance of metasurface-based optical beam scanning devices, we expect that the proposed Q3D-SWS will enable the development of miniaturized optical beam scanning devices with high efficiency, a large FOV, and high scanning speed. As the proposed Q3D-SWS performs best under normal incidence, an uncoaxial beam scanning system was employed to demonstrate high-efficiency half-space optical beam scanning. A schematic diagram of the uncoaxial beam scanning system is depicted in Fig. 4a. Notably, the two deflectors do not need to be positioned at a significant distance; a separation of just a few wavelengths is sufficient. This has minimal impact on the complexity and volume of the system. The experimental details of the scanning system are provided in Supplementary Information 9. In the beam scanning experiments, the two Q3D-SWSs in the system are identical. The rotation of the first Q3D-SWS enables an azimuthal rotation of the laser beam at a constant angle, which equals the deflection angle of the Q3D-SWS. Likewise, the rotation of the second Q3D-SWS allows the laser beam to reach different points by overlapping the scanning cone onto the scanning cone of the first Q3D-SWS. The deflection angle (θ) of the Q3D-SWS determines the outermost range of the scanning trajectory. The maximum scanning angle of the uncoaxial beam scanning system is equal to twice the deflection angle of the Q3D-SWS.

While the rotational motor and/or the Q3D-SWS are rotated, the incident light alternates between the TE and TM polarizations. To improve the efficiency of the beam scanning system, selecting a sample and wavelength with the highest non-polarization efficiency is crucial. The scanning video for 1550 nm, featuring a deflection angle of 42.4° (equivalent to a 170° × 170° FOV), is presented in Supplementary Video 1. Spurious diffraction results in a three-spot scanning pattern. To minimize the impact of spurious diffraction, we selected a wavelength of 1350 nm for beam scanning (refer to Supplementary Video 2). At this wavelength, the deflection angle is approximately 36°, and the maximum elevation angle reaches 72° (equivalent to a 144° × 144° FOV), providing a sufficiently large range to approach half-space conditions. The maximum optical efficiency of the beam scanning system can reach approximately 86.5%.

Figure 4b–d display the experimental results of the scanning patterns generated by cascaded Q3D-SWSs at different rotational speeds. More experimental results are provided in Supplementary Information 10. As shown in Fig. S13a, b, individual rotation of the first

https://doi.org/10.1038/s41467-025-58502-1

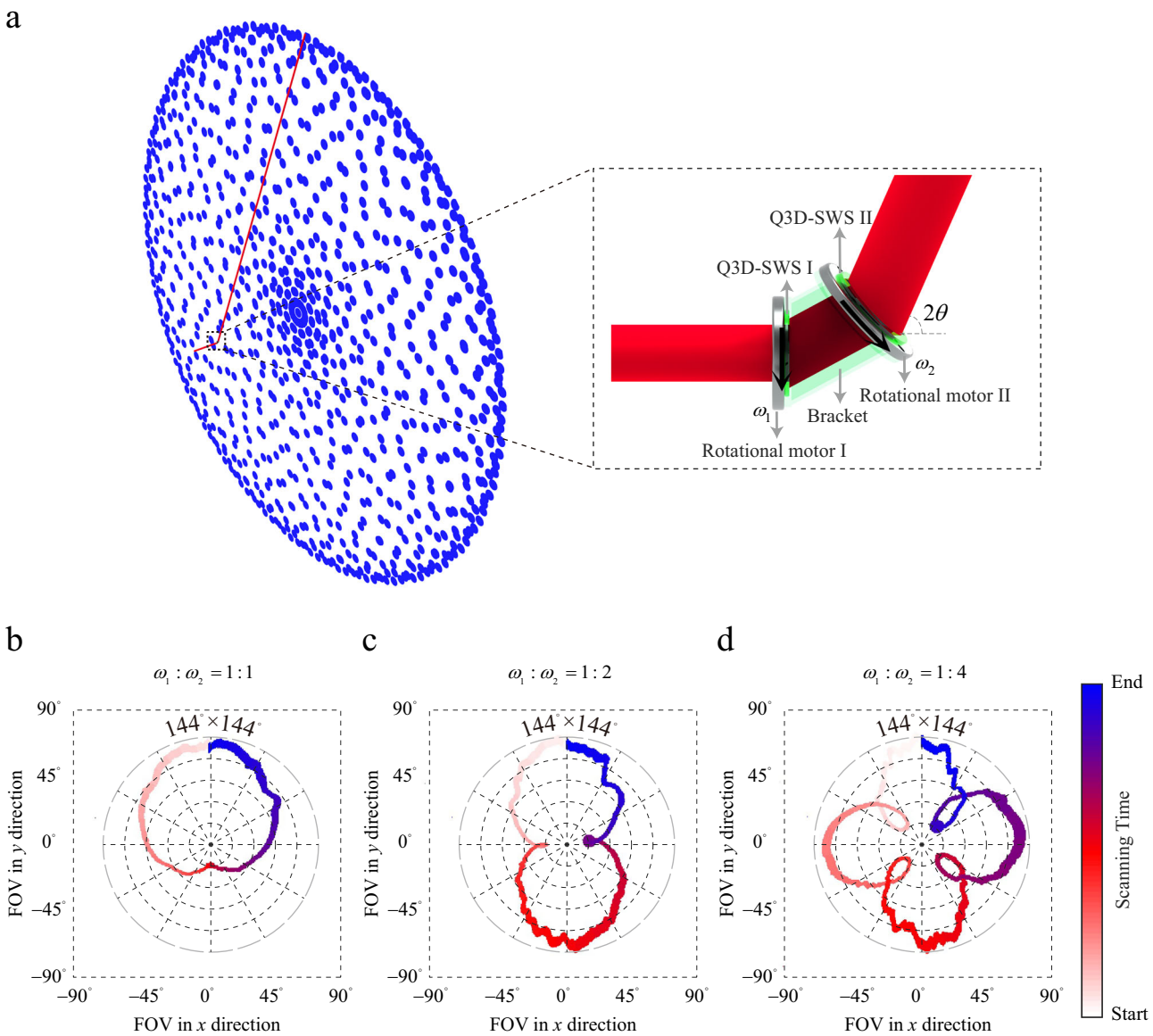

Fig. 4 | Optical beam scanning with cascaded quasi-three-dimensional subwavelength structures. a Schematic diagram of the optical beam scanning system. θ is the deflection angle of the quasi-three-dimensional subwavelength structure. ω_1 and ω_2 are the rotational speeds of rotational motors I and II, respectively. The blue scatters represent the scanning points when ω_1:ω_2 = 1:30. **b**–**d** Experimental results of scanning patterns generated by cascaded quasi-three-dimensional subwavelength structures at different rotational speeds (ω_1:ω_2). The colored bar represents the temporal evolution of the scan.

or second Q3D-SWS results in circular or elliptical scanning patterns. As illustrated in Fig. 4b–d and Fig. S13c–e, the initial positioning of the two Q3D-SWSs influences the starting point of the scanning patterns. The deviation angle of the two Q3D-SWSs induces the rotation of the scanning patterns. Additionally, as the rotational speed ratio decreases (ω_1:ω_2), the scanning pattern becomes denser, and the number of petals increases. Dense scanning trajectories result in higher scanning resolution. Nevertheless, these denser trajectories also prolong the scanning period. In practical applications, making a judicious choice based on the desired scanning resolution requirements and scanning speed is crucial.

Discussion

The paramount challenge in achieving optical beam scanning with both high efficiency and a large FOV lies in attaining anomalous refraction metasurfaces with perfect efficiency. However, single-layer metasurfaces, even those employing freeform geometries with maximum lateral freedom, struggle to achieve perfect anomalous refraction in the optical frequency domain, primarily because of inevitable reflection loss and/or spurious diffraction. To address this, we propose leveraging a Q3D-SWS to enhance longitudinal degrees of freedom, arousing a multiple scattering process to optimize symmetry breaking. We have successfully demonstrated perfect anomalous refraction using a Q3D-SWS and showcased high-efficiency half-space beam scanning through cascaded Q3D-SWSs. The actual scanning trajectory is entirely determined by the Q3D-SWSs and rotation parameters, remaining independent of the detection process. During the scanning experiments, the curtain is positioned very close to the scanning system to minimize the scanning area and ensure complete capture of the trajectory. However, the soft texture of the white curtain may introduce a slight deformation in the trajectory, as recorded by the infrared camera. We made efforts to keep the curtains as flat as possible during the experiment to minimize distortion, and this effect could be further mitigated by using a curtain with a harder texture.

Moreover, the use of miniature light sources and advanced mechanical systems allows for the development of a miniaturized, high-performance beam scanning system with the potential to revolutionize light detection and ranging systems and equipment.

In conclusion, to the best of our knowledge, we have achieved perfect anomalous refraction for the first time (see more details in Table S5), with a polarization-insensitive absolute efficiency exceeding 99%, through the construction of an all-dielectric Q3D-SWS. By utilizing a multilayer film with specific phase responses, which exhibits high transmittance to zeroth-order propagating waves and high reflectance to first-order propagating waves, we successfully suppressed reflection loss and spurious diffraction. Furthermore, we experimentally showcased an uncoaxial beam scanning system employing cascaded Q3D-SWSs, achieving 86% maximum efficiency in beam scanning with a FOV of 144° × 144°. Our proposed paradigm for perfect anomalous refraction is compatible with active[26] and temporal tuning[34], which can further enhance the performance of tunable metasurface-based optical beam scanning, particularly in terms of efficiency and FOV. Our work opens new opportunities for the development of high-efficiency metasurfaces, which are crucial for their commercialization and practical applications. Furthermore, our work may inspire the creation of high-performance meta-devices or meta-systems across various application scenarios.

Methods

Sample fabrication

Magnetron sputtering deposition, electron beam lithography, and inductively coupled reactive ion etching were used for deposition, patterning, and etching, respectively. The Si/SiO_2 multilayer films, SiO_2 spacer, and Si film were deposited using the NSC-15 magnetron sputtering deposition system from Optorun. The detailed deposition parameters can be obtained from our previous work[38]. The refractive indices of Si and SiO_2 are shown in Fig. S7 in the Supplementary Information. Following deposition, the substrate was spin-coated with a positive electron beam resist (Zep 520) at 4000 r.p.m. for 60 s and then baked on a hotplate at 180 °C for 5 minutes. The final thickness was approximately 240 nm. The sample was subsequently subjected to electron beam lithography using a 100-kV acceleration voltage (Raith 5200 system). The exposed resist was successively developed in amyl acetate for 60 s and isopropyl alcohol for 30 s. Reactive ion etching on the Oxford PlasmaPro100 Cobra was conducted using a gas mixture of SF_6 and CHF_3 (at flow rates of 15 and 50 sccm, respectively) under a pressure of 15 mTorr. The ICP power was set at 800 W, and the substrate bias was −380 V. The resist mask was then removed using oxygen plasma.

Optical beam scanning demonstration

A supercontinuum source SC-5 from YSL Photonics generated broadband incident light, which was then collimated by the fiber collimator and filtered to produce monochromatic light. Two identical Q3D-SWSs were mounted in stepper motors from Beijing Optical Century Instrument Co., Ltd., which were controlled by stepper motor controllers. Rotational motor II was mounted on a self-designed mechanical system, with a bracket positioned between the two rotational motors to ensure the vertical incidence of the light beam emitted from the first Q3D-SWS onto the second Q3D-SWS. The large FOV of the beam scanning system presented certain challenges in regard to detecting the scanning patterns. Typically, the FOV of an infrared camera is not sufficiently wide (55° × 43° in our experiment). To overcome this limitation, a large white curtain (2 m × 2 m) was placed approximately 10 cm away from the second Q3D-SWS, and an infrared camera positioned 1.2 m from the curtain captured the scanning pattern. This arrangement allowed us to capture the comprehensive scanning results within a single FOV. Relative efficiency refers to the ratio of the anomalous refraction energy to the total transmitted light energy, while absolute efficiency denotes the ratio of the anomalous refraction energy to the incident light energy in both simulations and experiments. The expression for relative efficiency is given by: $Eff_{rel} = E^{+1}/(E^{-1} + E^{0} + E^{+1})$. Similarly, the expression for absolute efficiency is: $Eff_{abs} = E^{+1}/I_0$, where E^i denotes the energy of the *ith*-order diffracted light and I_0 represents the energy of the incident light.

Data availability

The data that support the findings of this study are provided in the Supplementary Information.

References

1. Chen, Y. et al. Observation of intrinsic chiral bound states in the continuum. *Nature* **613**, 474–478 (2023).
2. Dorrah, A. H. & Capasso, F. Tunable structured light with flat optics. *Science* **376**, eabi6860 (2022).
3. Yu, N. et al. Light propagation with phase discontinuities: generalized laws of reflection and refraction. *Science* **334**, 333–337 (2011).
4. Sun, S. et al. Gradient-index meta-surfaces as a bridge linking propagating waves and surface waves. *Nat. Mater.* **11**, 426–431 (2012).
5. Khorasaninejad, M. et al. Metalenses at visible wavelengths: diffraction-limited focusing and subwavelength resolution imaging. *Science* **352**, 1190–1194 (2016).
6. Tseng, M. L. et al. Vacuum ultraviolet nonlinear metalens. *Sci. Adv.* **8**, eabn5644 (2022).
7. Feng, C. et al. Diatomic metasurface for efficient six-channel modulation of Jones matrix. *Laser Photonics Rev.* **17**, 2200955 (2023).
8. Kim, I. et al. Pixelated bifunctional metasurface-driven dynamic vectorial holographic color prints for photonic security platform. *Nat. Commun.* **12**, 3614 (2021).
9. He, T. et al. Scattering exceptional point in the visible. *Light. Sci. Appl.* **12**, 229 (2023).
10. Yang, S. & Ndukaife, J. C. Optofluidic transport and assembly of nanoparticles using an all-dielectric quasi-BIC metasurface. *Light. Sci. Appl.* **12**, 188 (2023).
11. Faraji-Dana, M. et al. Compact folded metasurface spectrometer. *Nat. Commun.* **9**, 4196 (2018).
12. Yang, Z. et al. Generalized Hartmann-Shack array of dielectric metalens sub-arrays for polarimetric beam profiling. *Nat. Commun.* **9**, 4607 (2018).
13. Sun, S., He, Q., Hao, J., Xiao, S. & Zhou, L. Electromagnetic metasurfaces: physics and applications. *Adv. Opt. Photonics* **11**, 380 (2019).
14. Cai, X. et al. Dynamically controlling terahertz wavefronts with cascaded metasurfaces. *Adv. Photonics* **3**, 036003 (2021).
15. Thureja, P. et al. Array-level inverse design of beam steering active metasurfaces. *ACS Nano* **14**, 15042–15055 (2020).
16. Komar, A. et al. Dynamic beam switching by liquid crystal tunable dielectric metasurfaces. *ACS Photonics* **5**, 1742–1748 (2018).
17. Wang, Y. et al. 2D broadband beamsteering with large-scale MEMS optical phased array. *Optica* **6**, 557–562 (2019).
18. Chen, R. et al. A semisolid micromechanical beam steering system based on micrometa-lens arrays. *Nano Lett.* **22**, 1595–1603 (2022).
19. Wu, P. C. et al. Dynamic beam steering with all-dielectric electro-optic III-V multiple-quantum-well metasurfaces. *Nat. Commun.* **10**, 3654 (2019).
20. Juliano Martins, R. et al. Metasurface-enhanced light detection and ranging technology. *Nat. Commun.* **13**, 5724 (2022).
21. Kim, I. et al. Nanophotonics for light detection and ranging technology. *Nat. Nanotechnol.* **16**, 508–524 (2021).
22. Li, N. et al. Spectral imaging and spectral LIDAR systems: moving toward compact nanophotonics-based sensing. *Nanophotonics* **10**, 1437–1467 (2021).

23. Chase, A. F. et al. Airborne LiDAR, archaeology, and the ancient Maya landscape at Caracol, Belize. *J. Archaeol. Sci.* **38**, 387–398 (2011).
24. Choi, Y. et al. KAIST multi-spectral day/night data set for autonomous and assisted driving. *IEEE Trans. Intell. Transp. Syst.* **19**, 934–948 (2018).
25. Park, J. et al. All-solid-state spatial light modulator with independent phase and amplitude control for three-dimensional LiDAR applications. *Nat. Nanotechnol.* **16**, 69–76 (2020).
26. Berini, P. Optical beam steering using tunable metasurfaces. *ACS Photonics* **9**, 2204–2218 (2022).
27. Sokhoyan, R., Hail, C. U., Foley, M., Grajower, M. Y. & Atwater, H. A. All-dielectric high-Q dynamically tunable transmissive metasurfaces. *Laser Photonics Rev.* **18**, 2300980 (2024).
28. de Galarreta, C. R. et al. Nonvolatile reconfigurable phase-change metadevices for beam steering in the near infrared. *Adv. Funct. Mater.* **28**, 1704993 (2018).
29. Shaltout, A. M., Shalaev, V. M. & Brongersma, M. L. Spatiotemporal light control with active metasurfaces. *Science* **364**, eaat3100 (2019).
30. Chung, H. et al. Electrical phase modulation based on mid-infrared intersubband polaritonic metasurfaces. *Adv. Sci.* **10**, 2207520 (2023).
31. Li, S.-Q. et al. Phase-only transmissive spatial light modulator based on tunable dielectric metasurface. *Science* **364**, 1087–1090 (2019).
32. Kafaie Shirmanesh, G., Sokhoyan, R., Pala, R. A. & Atwater, H. A. Dual-gated active metasurface at 1550 nm with wide (>300 degrees) phase tunability. *Nano Lett.* **18**, 2957–2963 (2018).
33. Li, M., Hail, C. U., Biswas, S. & Atwater, H. A. Excitonic beam steering in an active van der Waals metasurface. *Nano Lett.* **23**, 2771–2777 (2023).
34. Sedeh, H. B., Salary, M. M. & Mosallaei, H. Adaptive multichannel terahertz communication by space-time shared aperture metasurfaces. *IEEE Access* **8**, 185919–185937 (2020).
35. Estakhri, N. M. & Alu, A. Wave-front transformation with gradient metasurfaces. *Phys. Rev. X* **6**, 041008 (2016).
36. Epstein, A. & Eleftheriades, G. V. Synthesis of passive lossless metasurfaces using auxiliary fields for reflectionless beam splitting and perfect reflection. *Phys. Rev. Lett.* **117**, 256103 (2016).
37. Díaz-Rubio, A., Asadchy, V. S., Elsakka, A. & Tretyakov, S. A. From the generalized reflection law to the realization of perfect anomalous reflectors. *Sci. Adv.* **3**, e1602714 (2017).
38. He, T. et al. Perfect anomalous reflectors at optical frequencies. *Sci. Adv.* **8**, eabk3381 (2022).
39. Sell, D., Yang, J., Doshay, S., Yang, R. & Fan, J. A. Large-angle, multifunctional metagratings based on freeform multimode geometries. *Nano Lett.* **17**, 3752–3757 (2017).
40. Fan, Z. et al. Perfect diffraction with multiresonant bianisotropic metagratings. *ACS Photonics* **5**, 4303–4311 (2018).
41. Patri, A., Kéna-Cohen, S. & Caloz, C. Large-angle, broadband, and multifunctional directive waveguide scatterer gratings. *ACS Photonics* **6**, 3298–3305 (2019).
42. Liu, Y. et al. Slanted TiO2 metagratings for large-angle, high-efficiency anomalous refraction in the visible. *Laser Photonics Rev.* **17**, 2200712 (2023).
43. Zhang, L. et al. Ultra-thin high-efficiency mid-infrared transmissive Huygens meta-optics. *Nat. Commun.* **9**, 1481 (2018).
44. Paniagua-Dominguez, R. et al. A metalens with a near-unity numerical aperture. *Nano Lett.* **18**, 2124–2132 (2018).
45. Khaidarov, E. et al. Asymmetric nanoantennas for ultrahigh angle broadband visible light bending. *Nano Lett.* **17**, 6267–6272 (2017).
46. Shalaev, M. I. et al. High-efficiency all-dielectric metasurfaces for ultracompact beam manipulation in transmission mode. *Nano Lett.* **15**, 6261–6266 (2015).
47. Zhou, Z. P. et al. Efficient silicon metasurfaces for visible light. *ACS Photonics* **4**, 544–551 (2017).

Acknowledgements

This work was supported by the National Natural Science Foundation of China (61925504, 62192770, 62305252, 62020106009, 62192771, 62192774, 62205249), National Key Research and Development Program of China (Grant No.2023YFF0615604), Science and Technology Commission of Shanghai Municipality (21JC1406100), Shanghai Municipal Science and Technology Major Project (2021SHZDZX0100), Shanghai Pilot Program for Basic Research, and Fundamental Research Funds for the Central Universities.

Author contributions

T.H. and X.C. conceived the idea. T.H., Z. Wang and X.C. supervised the project. T.H., C.L., and H.L. performed theoretical analysis, numerical simulations with assistance from L.X., Y.S., and Z. Wei. T.H. and C.F. performed sample fabrication with assistance from S.D. and J.Z. T.H. and D.L. performed optical measurements and optical beam scanning demonstration with assistance from X.D. All authors were involved in the discussion and analysis. T.H. wrote the manuscript with contributions from all authors.

Competing interests

The authors declare no competing interests.

Additional information

Supplementary information The online version contains supplementary material available at https://doi.org/10.1038/s41467-025-58502-1.

Correspondence and requests for materials should be addressed to Zhanshan Wang or Xinbin Cheng.

Peer review information *Nature Communications* thanks the anonymous reviewer(s) for their contribution to the peer review of this work. A peer review file is available.